Supporting information
Assessing Utilization Boundaries for Pt-based Catalysts in an Operating PEMFC

Michal Ronovsky[1], Lujin Pan[2], Malte Klingenhof[2], Isaac Martens[1], Lukas Fusek[3], Peter Kus[3], Raphael Chattot[4], Marta Mirolo[1], Fabio Dionigi[2], Harriet Burdett[5], Jonathan Sharman[5], Peter Strasser[2], Alex Martinez Bonastre[5], Jakub Drnec[1]*

[1] ESRF—The European Synchrotron, ID 31 Beamline, Grenoble, France
[2] Electrochemical Energy, Catalysis and Material Science Laboratory, Department of Chemistry, Technical University Berlin, Berlin, Germany
[3] Charles University, Faculty of Mathematics and Physics, Department of Surface and Plasma Science, V Holešovičkách 2, 180 00, Prague 8, Czech Republic
[4] ICGM, Univ. Montpellier, CNRS, ENSCM, 34095 Montpellier Cedex 5, France
[5] Johnson Matthey Technology Centre, Blount's Court, Sonning Common, Reading RG4 9NH, U.K.
** Corresponding author: Jakub Drnec, email: drnec@esrf.fr*

oh-PtNiIr faster kinetics and microstrain

Martens et al. showed that the width of the oxidation/reduction hysteresis loop decreases with slower scan rates due to the slow kinetics of redox processes in some materials [1]. Conducting XRD-CV with various scan rates (100, 50, 20) mV/s, we also find the narrowing of the oxidation/reduction loop for the Pt catalyst (Figure S1a). For Pt(JM) catalyst, reduction onsets stabilize at 0.9 V with a 20 mV/s scan rate and thus become the same as for the oh-PtNiIr catalyst. Nevertheless, the reduction window remains wider for Pt, as Pt(JM) is reduced only below 0.6 V, and oh-PtNiIr is reduced already above 0.6 V. However, the width of the oxidation/reduction loop of the oh-PtNiIr catalyst shows no dependence on the scan rate (Figure S1b). It shows that oxidation/reduction on the oh-PtNiIr catalyst is in equilibrium with the potential at all times and that the reduction kinetics is faster than in Pt(JM).

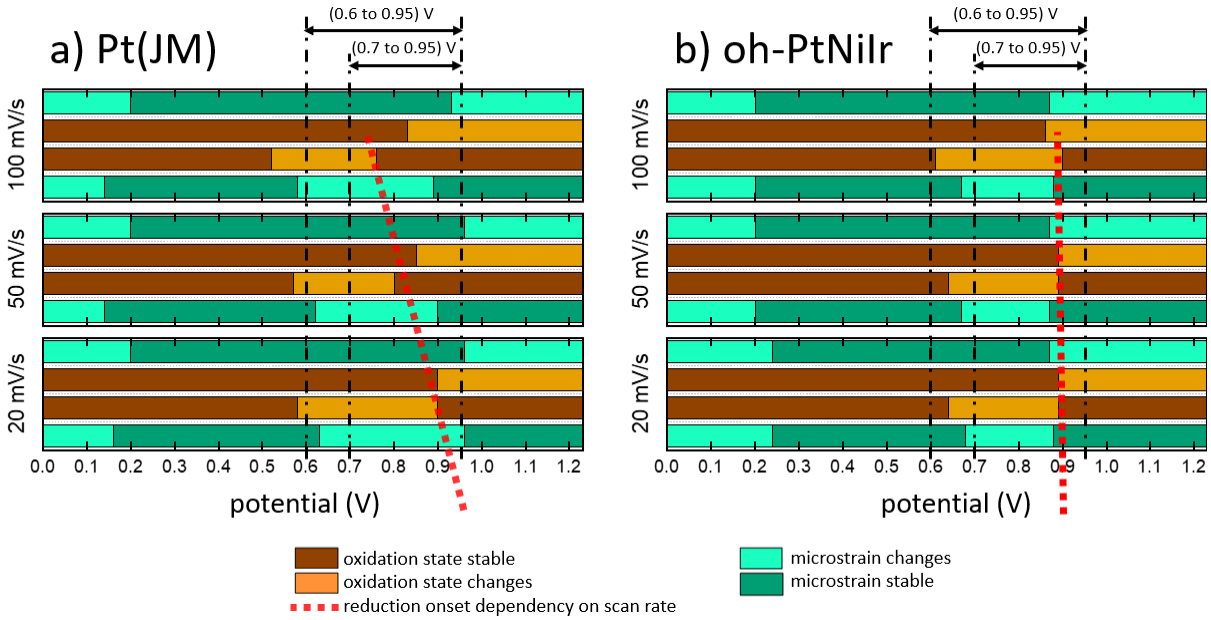

Figure S1: Simplified diagrams for a) Pt(JM) and b) oh-PtNiIr of scale factor (brown) and microstrain (green) in XRD-CV with three different scan rates (100, 50, and 20) mV/s. The red line connects the reduction onsets and shows the narrowing of the oxidation/reduction loop for Pt(JM), whereas oh-PtNiIr shows no such narrowing. Black dash-dot lines correspond to two types of ASTs used in this paper.

Faster kinetics are also observed by the analysis of microstrain. Microstrain originates from local defects in the lattice [2, 3]. Such defects can be generated by various surface processes and through diffusion distributed in the bulk of the NP, giving rise to the broadening of the diffraction peaks [3, 4]. One mechanism causing the microstrain increase is the so-called “place exchange,” where the structural defects are formed during the extraction of the Pt atoms [5, 6, 7, 8, 9, 10, 11]. Another possibility is the dissolution of less noble metals from alloyed NPs, which leaves defects throughout the bulk of nanoparticles [12].

Figure S2 adds the general trend of microstrain, distinguishing between the formation of amorphous surface oxide and other processes causing the increase of general disorder of atoms within the NPs. Such processes can be triggered by a place exchange during the oxidation onset, in which the localized surface strain caused by Pt-O swap, or dealloying where defects formed due to the Ni dissolution, inhomogeneously propagates to the bulk of the particle [4]. Microstrain follows a similar trend as the scale factor: it is constant in the (0.3 to 0.9) V range and then increases until sweep reversal. Upon reversal, it holds its value, and after the 0.9 V is crossed, it starts to decrease again until it reaches a plateau at 0.6 V. No difference between anodic and cathodic microstrain onsets is observed. An additional feature is present in the range of (0.05 to 0.3) V, where microstrain drops to its lowest value at 0.05 V. This part is associated with the hydrogen underpotential deposition region, in which adsorbed hydrogen likely further reduces and anneals the surface and, subsequently, the bulk of NPs, leaving behind a fully reduced catalyst.

For Pt(JM), microstrain onset is at higher potentials than scattering intensity onset (upper part in Figure S2). This might be due to the fact that a sufficient amount of amorphous oxide must be present on the surface before the surface microstrain propagates to the bulk and is, therefore, detectable by X-ray measurement. For oh-PtNiIr, microstrain increases in the anodic scan even before the formation of the amorphous oxide. This might be due to the preferential oxidation of Ni atoms [13, 14], with the suggested formation of subsurface Ni-O species [15], leaving behind structural defects even before the Pt-O place exchange kicks in. Additionally, it is likely that only a small amount of Ni-O species is necessary to trigger defect propagation into the bulk as the oh-PtNiIr catalyst has intrinsically higher microstrain due to alloying. The potential window of the microstrain decrease in the cathodic scan is shorter, giving another point that the relaxation processes are faster for oh-PtNiIr. Considering that the Ni-O bond is weaker than Pt-O [13], faster overall kinetics likely translates to faster Ni-O reduction (and dissolution) compared to Pt-O. Consequently, oh-PtNiIr alloy pays the price for better kinetics by its sensitivity to secondary metal leaching while cycling. The reduction of oh-PtNiIr at higher potentials also points to a need for tighter operational boundaries compared to a pure platinum catalyst.

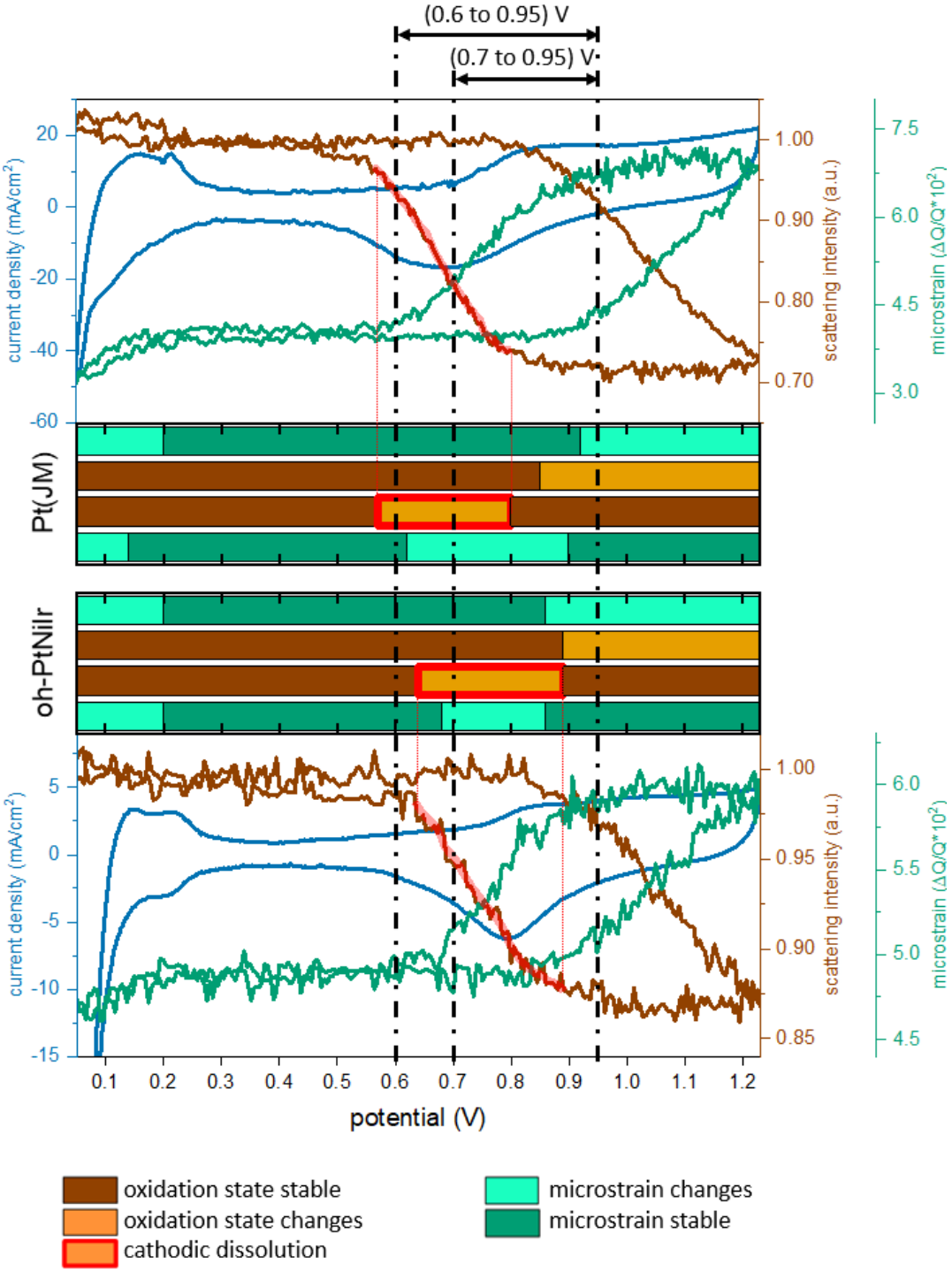

Figure S2. X-ray diffraction coupled with cyclic voltammetry. Scale factor (brown) and microstrain (green) were obtained with XRD during (0.05 to 1.23) V CV with a 50 mV/s scan rate. The upper half corresponds to the Pt(JM) and the lower part to the oh-PtNiIr. An increase in defect concentration during oxidation increases the microstrain value. The catalyst's oxidation is accompanied by a reversible decrease in scattering intensity. In the raw data, the cathodic dissolution region is highlighted by a red curve that extends into a simplified diagram where the dissolution region is highlighted by a red box. Black vertical dash-dot lines mark the potential boundaries of two types of ASTs to connect XRD-CV with long-term stability.

The effects of catalyst parameters on observed trends of scattering intensity and microstrain

To compare the catalyst with each other, it is important to describe the expected effects of various catalyst parameters on the trends of scattering intensity and microstrain observed in the main manuscript and in the chapter above. We will go through several parameters one-by-one. All the parameters have an impact on the lifetime durability of the device. Nevertheless, the important conclusion drawn in this manuscript is that the dissolution is proportional to the extent of reduction, and it is independent of particle size, shape, alloying, carbon type, etc.

Catalyst composition has a direct impact on the stability of the catalyst, affecting the transition metal leaching and particle size increase over its lifetime. Consequently, it will affect the hysteresis loop of scattering intensity and microstrain. If the redox kinetics are fast, the hysteresis loop does not change with the scan rate (Figure S1). The specific onsets of oxidation/reduction and microstrain will change with composition due to the different strengths of metal-oxygen bonds and different defect propagation, making, e.g., the reduction region wider.
Carbon type can affect the absolute value of scattering intensity as higher surface area carbon might expose more NPs, leading to higher utilization and, thus, larger scattering intensity drop when a larger amount of the catalyst is oxidized (averaged by X-rays).
Initial loading of the electrode can affect the utilization factor of the catalyst with the effects mentioned above.
Smaller **particle size** will primarily lead to a higher drop in scattering intensity when oxidized because the ratio of surface-to-bulk atoms is large, and the scattering intensity is an average over volume. It can also lead to a shift of onsets for oxidation/reduction and microstrain as the size affects catalytic activity.
Particle shape is closely related to the activity, so it will have an effect primarily on the onsets values, possibly introducing a shift with changing scan rate. We expect changes in the values and onsets of microstrain as defects within the NP will depend on its structure.
The **MEA preparation method** is crucial, as pointed out in the manuscript, because it heavily affects the composition, size, and shape of the NPs.
This is a limited list and one should note that there are certainly effects not known to us at this point.

Experimental

Catalyst powders

Johnson Matthey supplied carbon-supported Pt nanoparticles with average sizes of 2.9 nm as determined by XRD. The oh-PtNiIr catalyst powder was prepared on Vulcan XC72R by a seed-mediated solvothermal method (will be published separately). Two batches of ~500 mg each were prepared. The atomic composition of each batch, analyzed with ICP-OES, yielded $Pt_{68.2}Ni_{31.2}Ir_{0.5}$ and $Pt_{68.3}Ni_{31.3}Ir_{0.4}$ with Pt wt% of 30.1 and 29.0, respectively. For the first batch, TEM measurements showed a number-weighted nanoparticle size of (3.8 ± 1.6) nm. For the second batch, two particle sizes were identified. Bigger nanoparticles had the number-weighted NP size of (4.5 ± 1.7) nm, and smaller nanoparticles were (2.7 ± 1.7) nm in size. The volume-weighted nanoparticle size determined by XRD was 5.9 nm. A slightly larger volume-weighted NP size is a sign of non-symmetrical size distribution with the tail towards larger NPs, which is in line with the TEM of the second batch. Batches were mixed to make the ink for CCMs.

Ink-making

The cathode catalyst layers were prepared at an ionomer/carbon weight ratio of ca. 0.9/1, using Nafion 1100 Equivalent Weight ionomer. The inks were ball-milled for ca. 20 minutes before 24h aging. The inks were spray coated at ca. 10% solids onto Nafion 112 membrane.

Membrane electrode assemblies

CCMs printed from the catalyst powders were supplied by Johnson Matthey. For both types of CCMs, the anode is carbon-supported Pt with 0.079 mg_{Pt}/cm^2 loading. MEAs were prepared by cutting the CCM into 5 cm^2 pieces and aligning SGL 22BB GDL on both sides. For Pt(JM), the cathode loading is 0.187 mg_{Pt}/cm^2 with the average nanoparticle size determined by XRD of the CCM of 2.9 nm, showing no variation with the value estimated from the XRD of the raw catalyst powder. For oh-PtNiIr, the cathode loading was 0.100 mg_{Pt}/cm^2, 0.017 mg_{Ni}/cm^2, with the average nanoparticle size determined by XRD measurement of the CCM of 7.1 nm, so slightly larger than the value for the raw catalyst powder. This might be related to the increased NPs agglomeration observed in the TEM (Figure 1b), forming, in some cases, chains of several crystallites. Catalyst-coated membranes were fabricated using a hot-pressing decal transfer method within a temperature range of 160-180°C to combine the cathode catalyst layer, membrane, and anode catalyst layer. Loadings were measured with a desktop Fischer X-ray fluorescence machine FISCHERSCOPE® X-RAY XDV®-SDD.

Fuel cell and operation protocol

As-prepared MEAs were used in a custom fuel cell described in previous literature [16]. The cell was operated at 80 °C, with 80% relative humidity on the anode and cathode. MEAs for the XRD-CV experiments were conditioned at 0.6 V for approximately 2 h (Figure S3a). MEAs for the AST experiments were conditioned at constant current density for (1 to 3) h: oh-PtNiIr ”0.6 V LPL” at 140 mA/cm^2; ”0.7 V LPL” at 400 mA/cm^2; Pt(JM) ”0.6 V LPL” at 500 mA/cm^2; ”0.7 V LPL” at 500 mA/cm^2 (Figure S3b). In this case, constant potential conditioning was chosen to limit dissolution by oxidation and reduction. For both types of conditioning and the ASTs, the gas flow was 200/100 sccm O_2/H_2 with an additional 0.5 bar backpressure. For XRD-CV, the gas flow was 100/100 sccm N_2/H_2 with an additional 0.01 bar backpressure. We estimate that the difference between the inactive areas of the two oh-PtNiIr samples was less than 2 cm^2.

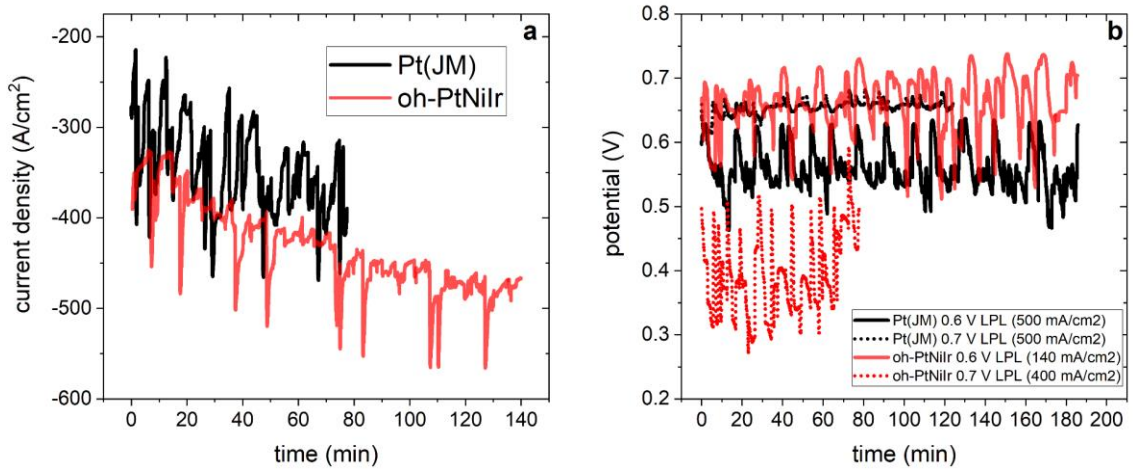

Figure S3: a) MEA conditioning of Pt(JM) and oh-PtNiIr MEA at 0.6 V for XRD-CV experiments. b) MEA conditioning for two types of ASTs 0.6 V LPL and 0.7 V LPL.

Electrochemistry

SP240 Biologic potentiostat was connected in the 4 electrodes setup. Voltage cables were connected directly to graphite flow fields, and the current was collected from the adjacent copper blocks [16]. Cyclic voltammetry was performed from 0.05 V to 1.23 V at 50 mV/s, flowing N_2/H_2 300/200 sccm at 80 °C, with 80% relative humidity. Ohmic resistance was measured with PEIS at 0.4 V from 100 mHz to 1 Hz. The protocol starts at 0.47 V, after compensation for ohmic drop at 85% amplitude. The first scan from 0.47 V to 1.23 V and back to 0.05 V is referred to as the 1st cycle. The second cycle shown in the Results and Discussion chapter starts at 0.05 V. Figure S4 shows scale factor (brown) and current density (blue) for the first two cycles for Pt(JM). We see that during the first cycle (dotted lines), scale factor decreases later in the anodic sweep, and thus the catalyst oxidizes at higher potentials than in the subsequent cycle. This is due to impurity desorption from an overall restructuring of the surface [17]. These impurities have to be removed by oxidation and reduction during the first cycle to get a clean surface that represents

the actual catalytic properties of the catalyst. It shows the importance of reporting at least the second cycle to obtain relevant electrochemical information. In our experiments, subsequent cycles had the same characteristics as the second cycle.

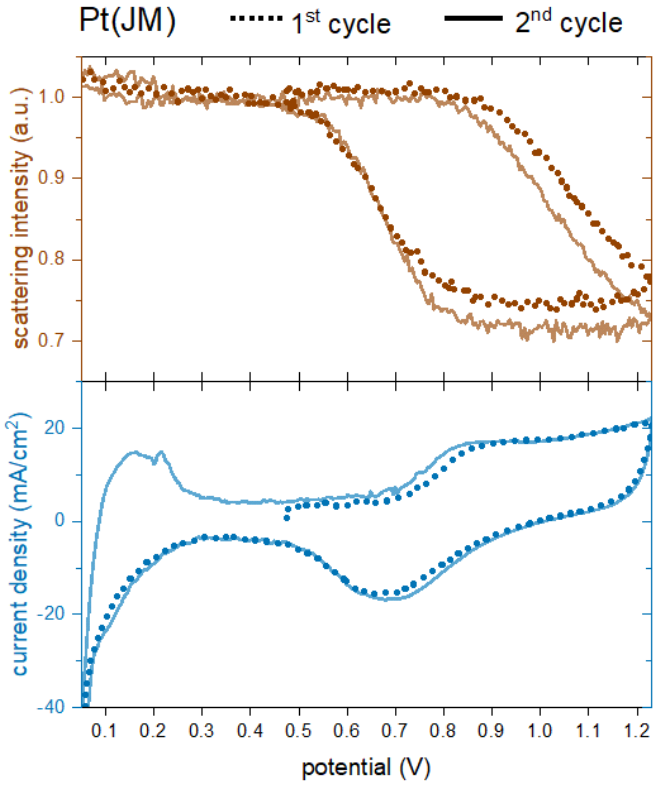

Figure S4: Differences between the 1st (dotted) and 2nd (line) cycle in XRD-CV for Pt(JM), scattering factor (brown), and current density (blue)

Accelerated stress tests were performed with SP240 Biologic potentiostat, flowing O_2/H_2 200/104 sccm at 80 °C, with 80% relative humidity and 0.5 bar backpressure. The total number of 10k cycles with either (0.6 to 0.95) V or (0.7 to 0.95) V were performed.

Electrochemical surface area (ECSA) was calculated from the H_{upd} desorption region of the CV before and after AST. Mass and specific activities (MA, SA) were estimated from the polarization curves at 0.9 $V_{iR\text{-}free}$ (Figure S5). For Pt(JM) 0.7 V, the ESCA fell from 77.8 m^2/g_{Pt} to 69.7 m^2/g_{Pt}, while MA and SA show a slight increase from 0.130 A/mg_{Pt} to 0.146 A/mg_{Pt}, and from 0.168 mA/cm^2_{Pt} to 0.210 mA/cm^2_{Pt}, respectively. For oh-PtNiIr 0.7 V, the ESCA fell from 29.2 m^2/g_{Pt} to 26.2 m^2/g_{Pt}, while MA and SA show a slight increase from 0.143 A/mg_{Pt} to 0.151 A/mg_{Pt}, and from 0.500 mA/cm^2_{Pt} to 0.576 mA/cm^2_{Pt}, respectively. Due to time constraints during the beamtime, we do not have datasets for both catalysts with 0.6 V LPL AST.

The polarization curves from the beginning of life (BOL) and the end of life (EOL) are in Figure S5. However, we do not have the polarization curve of sample oh-PtNiIr 0.6 V LPL due to time constraints during the beamtime. The polarization curves do not match the expected current densities because the cell is designed for X-ray diffraction experiments and compromises with flowfield design were made, and the cell is prone to flooding as a result. The polarization curves are normalized by the total 5cm^2 area, but some parts of the cell might be flooded. Consequently, the cell lacks reproducibility in terms of performance. Once flooded, it either has to be disassembled and dried. This is a lengthy process, many times unaffordable during beamtime, so we sacrifice a proportion of the active area of the CCM and thus performance. Nevertheless, as seen from the XRD-CV, we measure diffraction on the active part of the CCM.

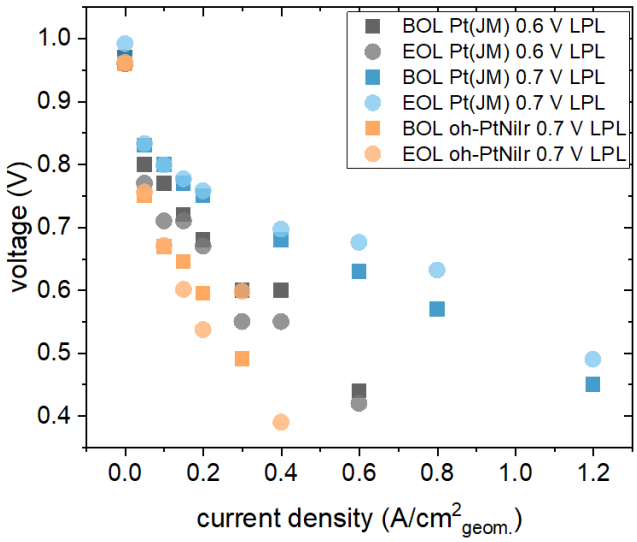

Figure S5: Polarization curves at the beginning and at the end of life for Pt(JM) 0.6 V LPL, Pt(JM) 0.7 V LPL, and oh-PtNiIr 0.7 V LPL. We do not have polarization curves for oh-PtNiIr 0.6 V LPL due to time constraints during the synchrotron utilization.

X-ray diffraction

XRD data were collected at the ID31 beamline at the European Synchrotron Radiation Facility. A 2D Pilatus 2M CdTe detector was used at a distance of 0.95 m from the sample. The photon wavelength was 0.161 Å (77.00 keV), just below the Pt K-edge. The beam size was approximately 5 × 20 µm (vertical x horizontal) with a flux of 10^{13} photons/s. The exposure time was 1 s per point for AST data and 0.1 s per point for XRD-CV. No significant beam damage was detected. Raw diffraction patterns (Figure S5a) were radially integrated using PyFAI [18]. Integrated 1D powder diffractograms were loaded into GSAS-II, and sequential Rietveld analysis was performed (Figure S5b) [19].

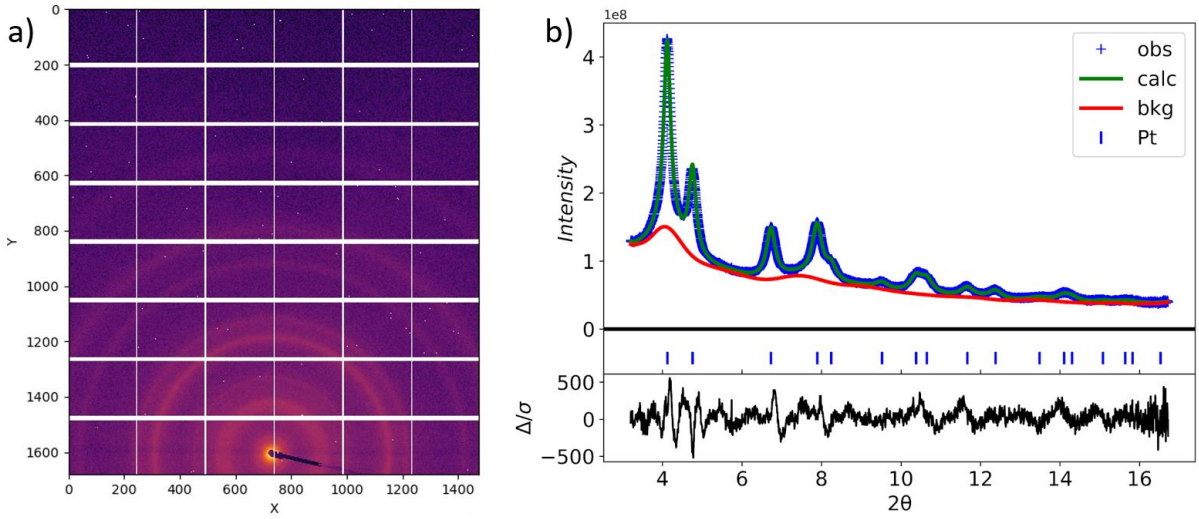

Figure S6: a) A diffraction pattern of oh-PtNiIr captured by the Pilatus 2M CdTe detector, b) Rietveld analysis of oh-PtNiIr radially integrated diffraction pattern.

Transmission electron microscopy

The measurements were conducted using a Tecnai G2 20 s-Twin microscope, equipped with a LaB6-cathode and a GATAN MS794 P CCD-detector at ZELMI Centrum, Technical University of Berlin. TEM samples were ultrasonicated in i-PrOH and drop-dried on copper grids.

Inductively Coupled Plasma Optical Emission Spectrometry

ICP-OES was used to determine the elemental composition of the various catalysts. Samples were prepared by dissolving 5 mg of the catalyst powder with 20 mg of $NaClO_3$ in a mixture of HCl and HNO_3 (3:1). The solutions were kept for 20 min at 180 °C using a Microwave Discover SP-D (CEM Corporation). The heating ramp was 15 °C/min. Subsequently, the solutions were diluted with Milli-Q® water, filtered, and brought to a known volume. To calculate the concentration of the different solutions, five standards of Pt, Ni, and Ir were prepared with concentrations of (1, 2, 7, 12, 20) mg/L for each element.

Energy-dispersive X-ray

EDX was carried out using XFlash 6|10 spectrometer (Bruker) installed within the MIRA III scanning electron microscope (Tescan). The primary electron beam energy was 20 keV. The area for spectra acquisition was 150um x 150um. Additionally, an area of 1000um x 1000um was used to rule out local inhomogeneities. EDX was used to determine elemental composition within oh-PtNiIr samples shown in Figure S6: as-prepared powder, fresh CCM, and aged CCM after 10k cycles of (0.6 to 0.95) V AST. PB-ZAF approach was used for peak deconvolution.

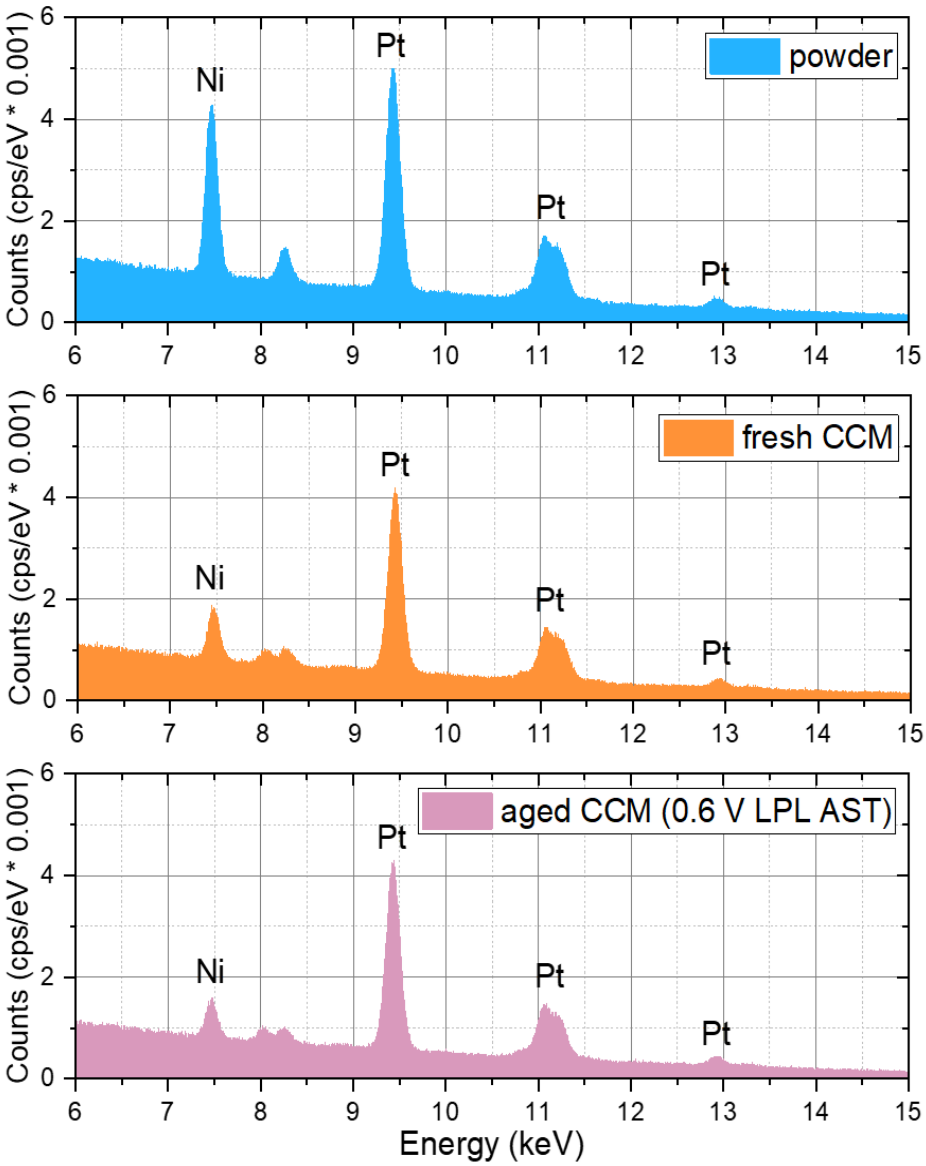

Figure S7: EDX of the synthesized powder, fresh CCM, and aged CCM after 10k cycles of (0.6 to 0.95) V AST

Raw data

The data used in this manuscript can be obtained upon request [20, 21].

References

(1) Martens, I.; Chattot, R.; Rasola, M.; Blanco, M. V.; Honkimäki, V.; Bizzotto, D.; Wilkinson, D. P.; Drnec, J. Probing the Dynamics of Platinum Surface Oxides in Fuel Cell Catalyst Layers Using in Situ X-Ray Diffraction. *ACS Appl. Energy Mater.* **2019**, *2* (11), 7772–7780.

(2) Leineweber, A. Understanding Anisotropic Microstrain Broadening in Rietveld Refinement. *Z. Kristallogr.* **2011**, *226* (12), 905–923.

(3) Chattot, R.; Le Bacq, O.; Beermann, V.; Kühl, S.; Herranz, J.; Henning, S.; Kühn, L.; Asset, T.; Guétaz, L.; Renou, G.; Drnec, J.; Bordet, P.; Pasturel, A.; Eychmüller, A.; Schmidt, T. J.; Strasser, P.; Dubau, L.; Maillard, F. Surface Distortion as a Unifying Concept and Descriptor in Oxygen Reduction Reaction Electrocatalysis. *Nat. Mater.* **2018**, *17* (9), 827–833.

(4) Kawaguchi, T.; Komanicky, V.; Latyshev, V.; Cha, W.; Maxey, E. R.; Harder, R.; Ichitsubo, T.; You, H. Electrochemically Induced Strain Evolution in Pt-Ni Alloy Nanoparticles Observed by Bragg Coherent Diffraction Imaging. *Nano Lett.* **2021**, *21* (14), 5945–5951.

(5) Drnec, J.; Ruge, M.; Reikowski, F.; Rahn, B.; Carlà, F.; Felici, R.; Stettner, J.; Magnussen, O. M.; Harrington, D. A. Initial Stages of Pt(111) Electrooxidation: Dynamic and Structural Studies by Surface X-Ray Diffraction. *Electrochim. Acta* **2017**, *224*, 220–227.

(6) Fuchs, T.; Drnec, J.; Calle-Vallejo, F.; Stubb, N.; Sandbeck, D. J. S.; Ruge, M.; Cherevko, S.; Harrington, D. A.; Magnussen, O. M. Structure Dependency of the Atomic-Scale Mechanisms of Platinum Electro-Oxidation and Dissolution. *Nature Catalysis* **2020**, *3* (9), 754–761.

(7) Ruge, M.; Drnec, J.; Rahn, B.; Reikowski, F.; Harrington, D. A.; Carlà, F.; Felici, R.; Stettner, J.; Magnussen, O. M. Electrochemical Oxidation of Smooth and Nanoscale Rough pt(111): An in Situ Surface X-Ray Scattering Study. *J. Electrochem. Soc.* **2017**, *164* (9), H608–H614.

(8) Jacobse, L.; Rost, M. J.; Koper, M. T. M. Atomic-Scale Identification of the Electrochemical Roughening of Platinum. *ACS Cent Sci* **2019**, *5* (12), 1920–1928.

(9) You, H.; Zurawski, D. J.; Nagy, Z.; Yonco, R. M. In-situ X-ray Reflectivity Study of Incipient Oxidation of Pt(111) Surface in Electrolyte Solutions. *J. Chem. Phys.* **1994**, *100* (6), 4699–4702.

(10) Nagy, Z.; You, H. Applications of Surface X-Ray Scattering to Electrochemistry Problems. *Electrochim. Acta* **2002**, *47* (19), 3037–3055.

(11) You, H.; Nagy, Z. Oxidation-Reduction-Induced Roughening of Platinum (1 1 1) Surface. *Physica B Condens. Matter* **1994**, *198* (1), 187–194.

(12) Kongkanand, A.; Ziegelbauer, J. M. Surface Platinum Electrooxidation in the Presence of Oxygen. *J. Phys. Chem. C Nanomater. Interfaces* **2012**, *116* (5), 3684–3693.

(13) Politano, A.; Caputo, M.; Goldoni, A.; Torelli, P.; Chiarello, G. Segregation and Selective Oxidation of Ni Atoms in Pt3Ni(111) in a Low-Pressure Oxygen Environment. *J. Phys. Chem. C* **2013**, *117* (51), 27007–27011.

(14) Politano, A.; Chiarello, G. Unveiling the Oxidation Processes of Pt3Ni(1 1 1) by Real-Time Surface Core-Level Spectroscopy. *ChemCatChem* **2016**, *8* (4), 713–718.

(15) Lee, H. C.; Kim, B. M.; Jeong, C. K.; Toyoshima, R.; Kondoh, H.; Shimada, T.; Mase, K.; Mao, B.; Liu, Z.; Lee, H.; Huang, C.-Q.; Li, W. X.; Ross, P. N.; Mun, B. S. Surface Segregation and Oxidation of Pt3Ni(111) Alloys under Oxygen Environment. *Catal. Today* **2016**, *260*, 3–7.
(16) Martens, I.; Vamvakeros, A.; Chattot, R.; Blanco, M. V.; Rasola, M.; Pusa, J.; Jacques, S. D. M.; Bizzotto, D.; Wilkinson, D. P.; Ruffmann, B.; Heidemann, S.; Honkimäki, V.; Drnec, J. X-Ray Transparent Proton-Exchange Membrane Fuel Cell Design for in Situ Wide and Small Angle Scattering Tomography. *J. Power Sources* **2019**, *437* (226906), 226906.
(17) Chattot, R.; Roiron, C.; Kumar, K.; Martin, V.; Campos Roldan, C. A.; Mirolo, M.; Martens, I.; Castanheira, L.; Viola, A.; Bacabe, R.; Cavaliere, S.; Blanchard, P.-Y.; Dubau, L.; Maillard, F.; Drnec, J. Break-In Bad: On the Conditioning of Fuel Cell Nanoalloy Catalysts. *ACS Catal.* **2022**, 15675–15685.
(18) Kieffer, J.; Ashiotis, G. PyFAI: A Python Library for High Performance Azimuthal Integration on GPU. **2014**. https://doi.org/10.48550/ARXIV.1412.6367.
(19) Toby, B. H.; Von Dreele, R. B. GSAS-II: The Genesis of a Modern Open-Source All Purpose Crystallography Software Package. *J. Appl. Crystallogr.* **2013**, *46* (2), 544–549.
(20) Ronovsky, M.; Polani, S. Stability Investigation of ORR Catalyst with Operando X-Ray Diffraction, 2024. https://doi.org/10.15151/ESRF-ES-618961874.
(21) Ronovsky, M.; Fusek, L.; Myllymäki, M. Why Are Advanced Pt-Alloyed ORR Catalysts Much Better on Paper than Standard Pt NPs but Fail in Real Devices?, 2025. https://doi.org/10.15151/ESRF-ES-749929551.